



Article

Monitoring of Carbonated Hydroxyapatite Growth on Modified Polycrystalline CVD-Diamond Coatings on Titanium Substrates

Rocco Carcione ^{1,2,*}, Valeria Guglielmotti ¹, Francesco Mura ^{3,4} , Silvia Orlanducci ¹ and Emanuela Tamburri ^{1,5,*} 

¹ Dipartimento di Scienze e Tecnologie Chimiche & UdR INSTM di Roma, Università degli Studi di Roma “Tor Vergata”—Via della Ricerca Scientifica, 00133 Rome, Italy; valeria.guglielmotti@uniroma2.it (V.G.); silvia.orlanducci@uniroma2.it (S.O.)

² ENEA, Fusion and Technology for Nuclear Safety and Security Department, C.R. Casaccia, Via Anguillarese 301, 00123 Rome, Italy

³ Department of Basic and Applied Sciences for Engineering (SBAI), University of Rome “Sapienza”, Via Antonio Scarpa 14, 00161 Rome, Italy; francesco.mura@uniroma1.it

⁴ Center for Nanotechnology Applied to Industry (CNIS), University of Rome “Sapienza”, 00185 Rome, Italy

⁵ Center for Regenerative Medicine (CIMER), University of Rome “Tor Vergata”, Via Montpellier 1, 00133 Rome, Italy

* Correspondence: rocco.carcione@enea.it (R.C.); emanuela.tamburri@uniroma2.it (E.T.)

Abstract: Production of diamond coatings on titanium substrates has demonstrated as a promising strategy for applications ranging from biosensing to hard tissue engineering. The present study focuses on monitoring the nucleation and growth of bone-like carbonated-hydroxyapatite (C-HA) on polycrystalline diamond (PCD) synthesized on titanium substrate by means of a hot filament chemical vapor deposition (HF-CVD) method. The surface terminations of diamond coatings were selectively modified by oxidative treatments. The process of the C-HA deposition, accomplished by precipitation from simulated body fluid (SBF), was monitored from 3 to 20 days by Raman spectroscopy analysis. The coupling of morphological and structural investigations suggests that the modulation of the PCD surface chemistry enhances the bioactivity of the produced materials, allowing for the formation of continuous C-HA coatings with needle-like texture and chemical composition typical of those of the bone mineral. Specifically, after 20 days of immersion in SBF the calculated carbonate weight percent and the Ca/P ratio are 5.5% and 2.1, respectively. Based on these results, this study brings a novelty in tailoring the CVD-diamond properties for advanced biomedical and technological applications.

Keywords: CVD-diamond coatings; carbonated-hydroxyapatite; surface chemistry modification; hydroxyapatite precipitation



Citation: Carcione, R.; Guglielmotti, V.; Mura, F.; Orlanducci, S.; Tamburri, E. Monitoring of Carbonated Hydroxyapatite Growth on Modified Polycrystalline CVD-Diamond Coatings on Titanium Substrates. *Crystals* **2024**, *14*, 66. <https://doi.org/10.3390/cryst14010066>

Academic Editor: Yuri N. Palyanov

Received: 30 November 2023

Revised: 23 December 2023

Accepted: 27 December 2023

Published: 6 January 2024



Copyright: © 2024 by the authors. Licensee MDPI, Basel, Switzerland. This article is an open access article distributed under the terms and conditions of the Creative Commons Attribution (CC BY) license (<https://creativecommons.org/licenses/by/4.0/>).

1. Introduction

The unique combination of properties such as hardness, corrosion resistance, chemical inertness, biocompatibility and non-cytotoxicity provides diamond a great added value for applications ranging from optoelectronics to quantum sensing, from drug delivery to tissue engineering [1–8]. In this view, advances in technology are addressing the attention of the scientific community to the production, characterization and processing of synthetic diamonds. In fact, the crystal structure, size, shape, morphology, surface chemistry and physical properties of synthetic diamonds can be properly tuned through specific growth conditions and processes [9–14]. In this scenario, diamonds produced in form of films on various substrates through chemical vapor deposition (CVD) methods have demonstrated great potential in fields extending from engineering to biomedicine [14–18]. Specifically, CVD approaches to produce diamond coatings offer several advantages, including precise control of growth conditions, versatility of substrates and deposition over large areas. In this context, many efforts are dedicated to produce diamond layers on a variety of substrates such as silicon, titanium, niobium, tantalum, molybdenum and glassy carbon [2,14,19–21],

as well as the possibility to incorporate foreign species, such as Nd, N, Ti and hybrid Si-Ni entities, within the diamond lattice directly during the diamond growth [7,9,22,23]. In addition, CVD techniques have proven to be powerful tools to tailor crystallographic defects, sp^2 and amorphous carbon content, amount of grain boundaries and surface terminations (H, O) of diamond materials [24–26].

Among the possible substrates, titanium and its alloys (Ti_6Al_4V) have a competitive advantage over other systems thanks to an outstanding combination of electroconductivity, tensile strength, corrosion resistance and biocompatibility [27–30]. In particular, recent studies focused on the exploitation of diamond coatings on titanium substrates [27–30] for biomedical applications like biosensing [31], memristive devices [32], heart valves [33] and regenerative medicine [34–36]. Regarding the latter, CVD-diamond coatings have shown significant promise as scaffolds for hard tissue engineering [5,8,9,37]. In fact, diamond phase was not only demonstrated to behave as a chemical protection against the corrosion phenomena by body fluids, but also to produce a bone–implant interface enhancing the biocompatibility with respect to bare titanium substrates [3,5,38,39]. A great amount of the literature acknowledges that the controlled roughness, topography and surface composition of CVD-diamond layers can stimulate osteoblasts (i.e., bone-forming cells) to proliferate and differentiate [9,17,38], while few studies explored the ability of diamond to favor the formation of bone-like hydroxyapatite ($Ca_{10}(PO_4)_6(OH)_2$) mineral, which is generally considered as a proof of concept anticipating the biomaterials' osteointegration ability in vivo. In particular, Strąkowska et al. pointed out how homogeneity and electrical conductivity of diamond substrates play a key role on the electrochemical deposition of hydroxyapatite coatings [40]. Similarly, Fox et al. demonstrated that the in vitro exposure to simulated body fluid (SBF) enables apatite deposition onto unmodified PCD systems [9,41].

Among the possible methods for producing hydroxyapatite, the precipitation from SBF permits the formation of bone-like hydroxyapatite with a carbonate ions' amount reproducing the bone mineral stoichiometric composition [42–45]. Such a carbonated hydroxyapatite (C-HA) can be distinguished in type A or B depending on whether the carbonate group replaces the hydroxyl or phosphate group, respectively. When the replacement of PO_4^{3-} by CO_3^{2-} ions results in a Ca/P ratio of about 2.0, a C-HA analogous to that of biological apatite minerals is obtained [45–49]. Therefore, the development of synthesis strategies capable of providing B-type C-HA coatings with structure, morphology and chemical composition similar to those of the bone mineral can be considered of great interest for tissue engineering applications.

In this context, the present research is devoted to investigating how the bioactivity of CVD diamond can be purposely modulated by surface chemistry and topography for allowing the formation of C-HA with tailored compositional, morphological and structural features. To this aim, hot filament chemical vapor deposition (HF-CVD) was employed to synthesize PCD films on titanium substrates. The surface terminations of the diamond layers were selectively modified by oxidative treatments in air at 350 °C. Then, the growth of C-HA crystals by precipitation from SBF on diamond layers was monitored by means of Raman spectroscopy analysis after regular periods of time from 3 to 20 days. The obtained results evidenced that the modulation of polycrystalline diamond films' surfaces is crucial to enhance the deposition and growth of C-HA crystals with morphology and chemical composition similar to those of the bone-mineral.

Taken together, the collected results underline how the possibility of specifically controlling and modifying the synthesis conditions of CVD diamond allows the production of materials with functions that can be modulated in relation to the development needs of advanced and industrially scalable technological devices.

2. Materials and Methods

2.1. Chemicals

$HClO_4$, methanol, n-butanol, NaCl, $NaHCO_3$, KCl, K_2HPO_4 , $MgCl_2 \cdot 6H_2O$, $CaCl_2$ and Na_2SO_4 were purchased by Merck KGaA and used as received.

2.2. Diamond Films Synthesis and Processing

Titanium substrates were prepared by cutting a 0.5 mm thick polycrystalline titanium sheet in 1 cm × 1 cm squares which were flatted by a cylindric piston. To obtain a mirror-like surface, the titanium substrates were cleaned by electropolishing operation. The electropolishing solution was prepared by mixing 30 mL of 70% HClO₄, 295 mL of methanol and 175 mL of n-butanol [38]. Electropolishing process was performed at −30 °C, applying a potential of 20 V for 15 min. Titanium foils were connected to the anode, while plates of stainless steel were connected to the cathode. Before the CVD process, a seeding operation was carried out to encourage nucleation and growth of homogeneous diamond films on the titanium substrates. Each titanium sheet was subjected to a 15 min sonication cycle in a “seeding” solution of 50 mg nanodiamond powder in 20 mL ethanol and then washed in ethanol. To synthesize the diamond films, a 1.25:100 CH₄/H₂ mixture activated by a Joule-heated Ta filament was used. Filament temperature and chamber pressure were respectively held at about 2130 ± 10 °C and 36 ± 1 torr during all the synthesis process which lasted for three hours. To modify the surface composition, diamond films were annealed in air at 350 °C for 20 min. Annealed and pristine diamond films were named as “D_A” and “D” samples, respectively. Bare titanium sheets (Ti samples) were used as reference to monitor the apatite deposition.

2.3. Hydroxyapatite Precipitation

A 1.5 SBF with inorganic ions concentrations simulating human blood plasma was prepared following the methodology outlined by Kokubo et al. [50]. Specifically, chemical reagents such as NaCl (206 mmol), NaHCO₃ (6.3 mmol), KCl (4.4 mmol), K₂HPO₄ (1.5 mmol), MgCl₂·6H₂O (2.4 mmol), CaCl₂ (3.7 mmol) and Na₂SO₄ (0.8 mmol) were dissolved into distilled water at 37 °C. Then, the solution was buffered at pH 7.40 by using 1 M HCl. To ensure that no precipitation occurred before experimental use, the prepared 1.5 SBF was refrigerated at 4 °C overnight. Daily for 20 days, each sample was accurately washed and exposed by immersion to fresh SBF for the entire 24 h. Before the analyses, the samples were repetitively washed with distilled water and dried overnight in air and at RT.

2.4. Characterization Techniques

SEM, EDX, Raman spectroscopy and XPS techniques were utilized to characterize the synthesized materials.

A Zeiss Auriga 405 Field Emission Scanning Electron Microscopy (FESEM) (Zeiss Microscopy GmbH, Jena, Germany), equipped with a Bruker Quantax detector (Bruker, Berlin, Germany), was used to obtain the SEM images and EDS spectra, maintaining a pressure of about 10^{−5} to 10^{−6} mbar. The electron beam operated at a working distance of 6 mm, while the acceleration voltage was set at 10 keV for both imaging and collecting the EDX spectra. The collected images were processed by using Image J software.

An XploRA ONE™ Raman Microscope (Horiba Italia Srl, Rome, Italy) was employed to collect Raman spectra. Raman analysis was performed in order to evaluate the structural quality of the deposited diamond films. All the spectra were acquired with the laser source at 532 nm operating at 1% power, the grating set on 2400 grooves/mm and acquisition time of 20 s. Each single peak or band in the spectra was deconvolved with a Lorentzian line shape to derive position, intensity and full width at half maximum (FWHM) parameters.

XPS analysis was performed using a KRATOS Axis Ultra DLD apparatus (Kratos Axis Ultra DLD, Manchester, UK). An incident monochromatic X-ray beam from Al target (15 kV, 10 mA) was focused on sample surface. The angle between the X-ray emitter and the photoelectron detector direction was set at 0°. The electron energy analyzer was operated with a pass energy of 20 eV enabling the collection of high-resolution spectra. A step size of 0.05 eV was employed. The core level spectrum was deconvolved through Voigt functions, after performing a Shirley background subtraction.

All the characterizations are performed at RT.

3. Results

3.1. Diamond Films

SEM images and deconvolved Raman spectra of diamond layers grown on electropolished Ti substrates before (D) and after (D_A) annealing treatment are shown in the Figure 1.

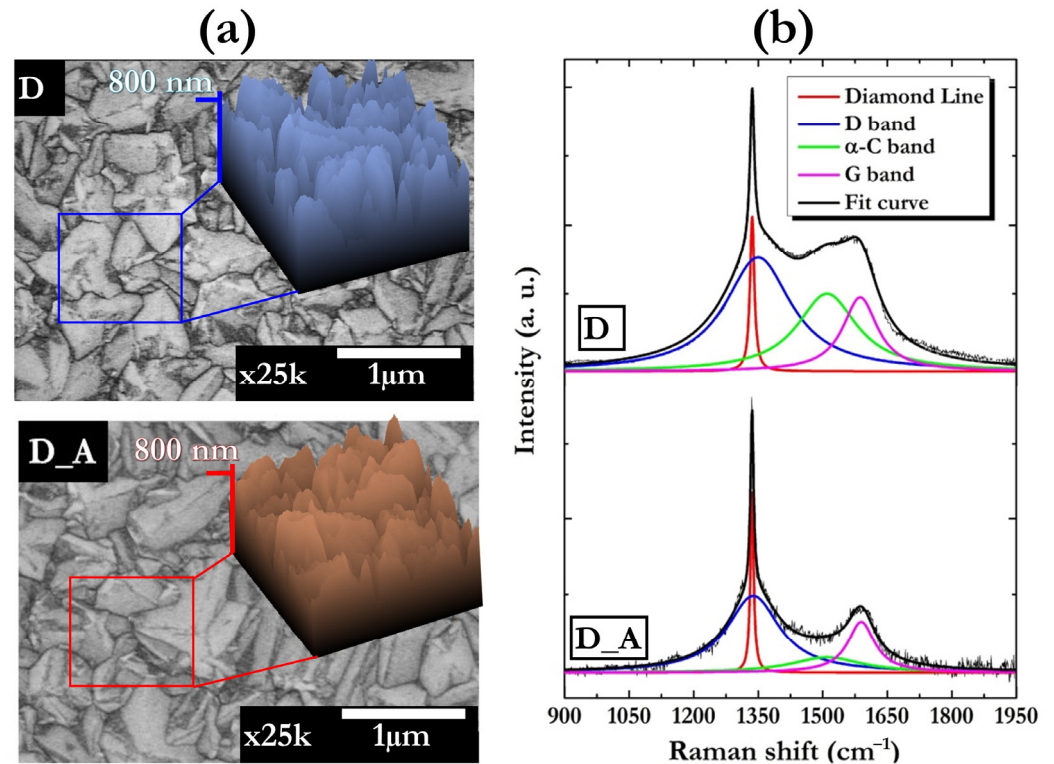


Figure 1. (a) SEM images and (b) deconvolved Raman spectra of pristine (D) and annealed (D_A) diamond samples. Insets: 3D SEM image and Raman signals attributions.

We can observe that both the samples exhibit a polycrystalline texture, constituted by triangularly faceted grains (Figure 1a). The high magnification images were processed through ImageJ software to obtain a 3D detailed reconstruction of the samples surface topography (inset in Figure 1a). The topographic investigation was carried out on $5 \mu\text{m} \times 5 \mu\text{m}$ squares areas. Averaged surface roughness (R_a) values were derived from the analysis of three different SEM images for each sample. This procedure provided for both D and D_A $R_a \sim 350 \text{ nm}$, which is a value comparable to the nanoscale architecture of natural tissues. From this result it is evident that the adopted annealing treatment produced no significant effects on the diamond topography. On the contrary, a different profile was detected for the Raman spectra of the two samples (Figure 1b) indicating that the thermal process induced structural modifications within the diamond phase. To better detail such an aspect, for each sample five different Raman spectra were collected and analyzed from different microregions. Each spectrum was deconvolved with four Lorentzian lines, that are the diamond line at around 1332 cm^{-1} and the D, G and amorphous carbon (α -C) bands at about 1350 , 1570 and 1510 cm^{-1} [51–53]. For each sample the diamond volume fraction (Σ_d) was also calculated following the procedure described in Refs [54]. Σ_d values of 92 and 96 were collected for D and D_A, respectively. In particular, the $I_{\text{DIA}} / I_{\alpha\text{-C}}$ ratio between the integrated intensities of diamond line (I_{DIA}) and α -C band ($I_{\alpha\text{-C}}$) ranges from 0.14 for D to 0.57 for D_A, strongly evidencing a considerable reduction in the amorphous carbon content due to the annealing treatment. Accordingly, the reduction from 13 to 10 cm^{-1} of the diamond line FWHM for D_A indicates an increase in the crystalline quality. Both these

results can be reasonably explained with the elimination of amorphous carbon content and sp^2 carbon phases at the boundaries of the nanometric diamond grains.

Further speculation can be made by considering the results of the XPS analysis. In Figure 2 typical spectral surveys (a) and representative deconvolved C 1s high-resolution spectra (b) along with the signals' attribution are reported for annealed D_A and reference D sample. The data were averaged on three spectra taken from different zones of each sample.

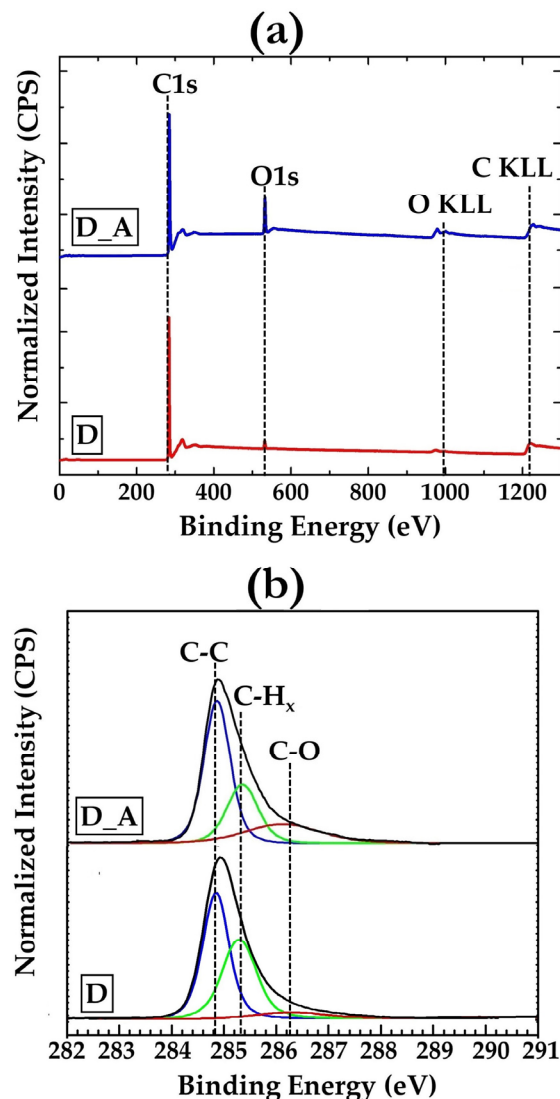


Figure 2. (a) Survey XPS spectra; (b) deconvolved high resolution C 1s spectra of D and D_A samples along with signals attribution (blue line: C-C bond signal; green line: C-H_x bond signal; red line: C-O bond signal).

The survey spectra were analyzed by referencing the peak related to the C 1s level of diamond at 285 eV [55,56]. In this view, the signal located at around 532 eV is assigned to the oxygen O 1s, reasonably due to carbon atoms in oxidized configurations. In perfect agreement with previous studies [31,38], no Ti signals are detected for both diamond layers, indicating that the adopted annealing method was successful in avoiding delamination phenomena. The quantitative analysis of the experimental data provides a surface elemental composition of about 98.5% C and 1.5% O for D sample. Conversely, around 90% C and about 10% O are found for D_A. To get a deeper insight into the surface chemical composition, the high-resolution C1s spectra were deconvolved by using three Voigt lines referring to C-C (284.8 eV), C-H_x (285.3 eV) and C-O bonds (286.3 eV) (Figure 2b) [55,57–59]. It is to

be noted that no titanium carbide neither C=C bonds signals are detected, corroborating the hypothesis that the thermal treatment was able to remove amorphous and graphitic carbon, without producing detachment of the diamond films from the underlying titanium substrates. Deconvolution procedure also allows determining the values of binding energy (BE), area and FWHM for each peak. The relative component concentrations (content percentage) are obtained from each sub-peak area of C 1s spectra. The relative concentrations of each component were determined from the corresponding sub-peak area by taking into consideration the Scofield sensitivity factors. The values are reported in Table 1.

Table 1. Percentage of C in the various configurations for the D and D_A sample.

Sample	C-C sp ³ (%)	C-H _x (%)	C-O (%)
D	56.4	42.1	1.5
D_A	54.2	36.3	9.5

We can note that the diamond layers exhibit a rather different surface composition. The larger degree of surface oxidation exhibited by D_A can be explained as due to the annealing treatment. At the temperature of 350 °C, the dangling and C-H_x bonds are in fact expected to interact with the air oxygen molecules, enabling the formation of surface C-O moieties.

3.2. Carbonated Hydroxyapatite Growth

To evaluate how the controlled introduction of oxygen-containing groups can modulate the ability of diamond surface to precipitate C-HA, D and D_A samples were soaked for 20 days in 1.5 SBF. The monitoring of C-HA formation was accomplished by means of Raman spectroscopy analysis performed as a function of exposure time to SBF (Figure 3) [45]. Three different Raman spectra were collected and analyzed from different microregions.

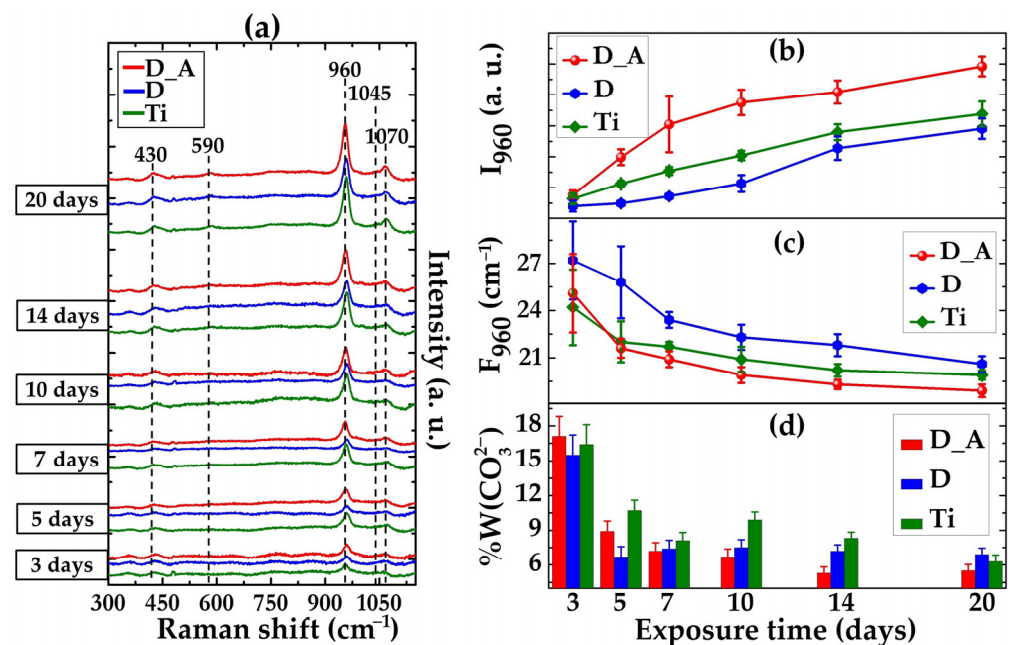


Figure 3. (a) From top to down: Raman spectra of apatite-like deposits acquired on D_A (green lines), D (blue lines) and Ti (red lines) substrates after exposure to 1.5 SBF for 3, 5, 7, 10, 14 and 20 days. Trend of: (b) I_{960} , (c) F_{960} and (d) $\%W(\text{CO}_3^{2-})$ values as a function of the exposure time. Error bars represent the standard deviation of the parameters derived by the deconvolution of three Raman spectra.

The Raman spectra show the typical signals of apatite-based minerals at about 430, 590, 960 and 1045 cm^{-1} , and which can be attributed to ν_2 , ν_4 , ν_1 and ν_3 PO_4^{3-} modes, respectively (Figure 3a) [60–63]. The peak at ~ 1070 cm^{-1} is attributable to the carbonate ν_1 mode in B-type sites, indicating the success in producing a mineral phase closely resembling biological apatite [60,64,65].

Upon closer observation of the spectra, one notices that the C-HA signals are better defined for D_A than for reference D and Ti supports. In details, the peak assigned to the ν_4 phosphate mode at about 590 cm^{-1} appears after 14 days for C-HA grown on D_A substrate, while such a signal can be observable only after 20 days of 1.5 SBF exposure for the other two substrates. These findings evidence that the annealed diamond promotes the achievement of a good apatite structural quality faster than both the bare titanium and the pristine diamond film. In addition, the lack of signals in the region between 1070 and 1110 cm^{-1} , typically ascribed to A-type C-HA, point out an almost complete substitution of carbonate ions in the B-sites of the apatite lattice [61,62,66].

In order to evaluate and compare the structural features and the amount of the C-HA deposits on the various substrates, the time evolution of the integrated intensity value (I_{960}) (Figure 3b) and of the band amplitude (FWHM_{960}) (Figure 3c) of the ν_1 phosphate mode were respectively monitored. As a general trend, the I_{960} and FWHM_{960} values monotonically increase and decrease, respectively, under exposure to 1.5 SBF. Specifically, we observe that I_{960} values of C-HA grown on D_A are systematically higher than those of the C-HA precipitated on reference D and Ti substrates at each investigated time of immersion. Analogously, FWHM_{960} values are found always lower for the C-HA deposited on D_A with respect to those of C-HA on D and Ti substrates. More in detail, for C-HA on D_A it is possible to observe a rapid and significant increasing in the I_{960} value between 3 and 7 days, while a rather gradual increase is noted between 10 and 20 days of SBF exposure. On the other hand, for C-HA on D a minimal change in the I_{960} value was detected between 3 and 5 days, while the signal intensity raises more rapidly between 5 and 20 days. In particular, a remarkable increasing can be observed between the 10th and 14th day of immersion, suggesting that the enrichment of the apatite-like nuclei occurs in this period of exposure. These different trends can be reasonably explained by taking into account the surface chemistry features, suggesting that the controlled introduction of oxygen-containing groups performed on D_A significantly reduces the time required C-HA to grow. Nonetheless, the crystalline quality of C-HA is very similar for all investigated substrates, as disclosed by the trend of the FWHM_{960} values (Figure 3c).

From Raman spectra it is also possible to achieve an indication on the carbonate content of C-HA by the Equation (1) derived by Spizzirri et al. [66]:

$$\%W(\text{CO}_3^{2-}) = \frac{\left(\frac{I_{1070}}{I_{960}}\right) - 0.05}{2.8} \times 100 \quad (1)$$

where $\%W(\text{CO}_3^{2-})$ is the carbonate weight percent and $\frac{I_{1070}}{I_{960}}$ is the ratio between the integrated intensities of the combined carbonate-phosphate (I_{1070}) and the phosphate ν_1 (I_{960}) peaks. The calculated $\%W(\text{CO}_3^{2-})$ values are reported in Figure 3d. We can note that for all three substrates the carbonate content is maximum after the first three days of C-HA formation with a variable value between 15 and 17%, and then constantly decreases and settles at day 20 at values between 5 and 7% which are similar to those of the natural inorganic mineral of human bones [63,67,68]. This trend can be explained by the lower solubility of calcium carbonate which initially enriches the first apatite nuclei generated by SBF, and subsequently consolidate their C-HA structure under the longer exposure times to the simulated body fluid.

Information about the morphology and elemental composition of the C-HA deposits were achieved by SEM-EDX analysis. In Figure 4 the results collected for D_A, D and reference Ti substrates after 20 days of immersion in 1.5 SBF are reported.

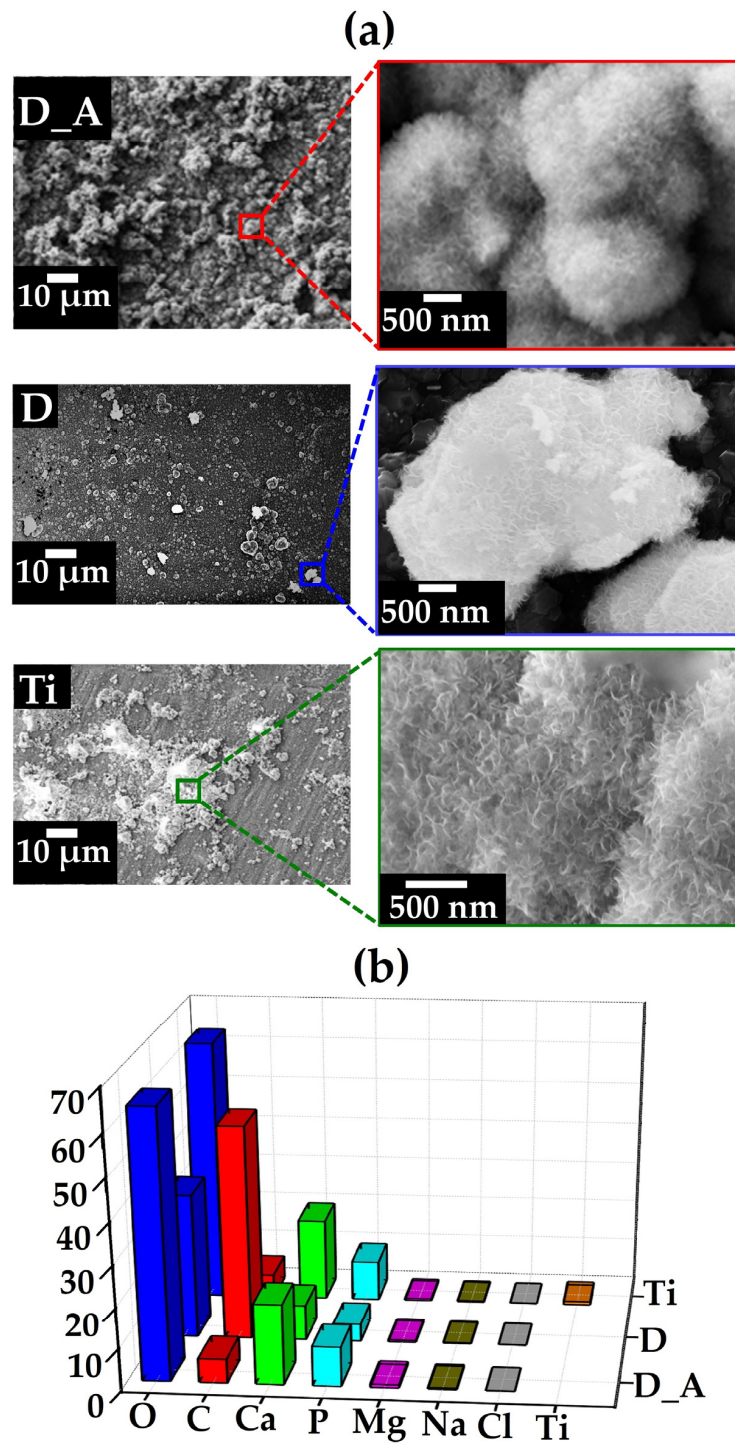


Figure 4. (a) SEM images and (b) histogram showing the elemental composition of C-HA deposits produced on D, D_A and Ti substrates after 20 days immersion in 1.5 SBF.

As shown in Figure 4a, the substrate strongly modulates the morphological features of the C-HA phase. In fact, Ti substrate produces a ‘patchy’ apatite-like deposition while the formation of sparse apatite globules sized around 1–5 μm is observed on D. Interestingly, a continuous and thick coating was indeed observed for D_A sample. As evidenced by the insets in the Figure 4a, all the C-HA crystals exhibit a needle-like texture, which is a fundamental requirement to induce osteogenic activities of bone forming cells [69].

The chemical composition and the Ca/P ratio values were evaluated by means of EDX spectroscopy by analyzing $3 \mu\text{m} \times 3 \mu\text{m}$ squares areas of the C-HA deposit. As a general

trend, the analysis shows that oxygen, carbon, calcium and phosphorous are the main components, while elements such as Na, Cl, Mg and K were detected only in traces. In line with SEM analysis, traces of Ti element (>0.8%) disclosed for C-HA on Ti are evidently due to the substrate, suggesting that the C-HA deposits' thickness is lower than 1 μm . Analogously, the consistent amount of carbon detected for C-HA on D plausibly arises from the uncoated diamond areas. It is worthy to note that a carbon percentage around 6% is detected for the C-HA on Ti and D_A substrates, corroborating the amount of carbonate ions derived by Raman spectroscopy analysis. The calculated Ca/P ratio are 2.11, 2.09 and 2.05 for C-HA on D_A, D and Ti, respectively. All these values are strictly close to those of human bone mineral [45–49], nevertheless the better structural and coating quality of C-HA on D_A can be explained by the interplay between the morphological, structural and surface chemistry features of the modified D_A diamond layer. A possible mechanism for the formation of C-HA crystals on the oxidized diamond surface of D_A is tentatively described in Figure 5.

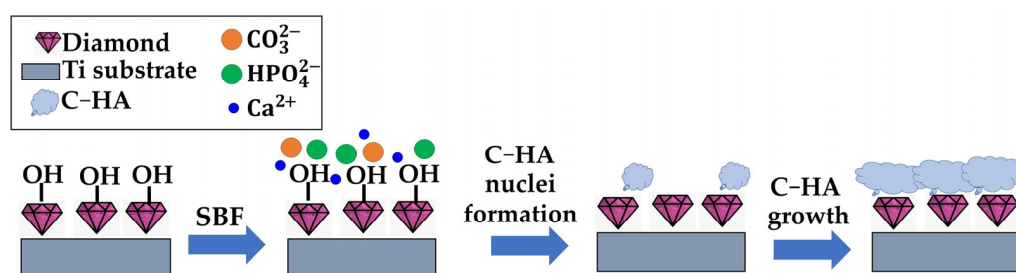


Figure 5. Schematic representation of a possible mechanism for the nucleation and growth of hydroxyapatite on the modified diamond layers. It should be noted that the representation does not take mineral's stoichiometry into account.

As disclosed by XPS analysis, D_A sample shows an $\sim 10\%$ amount of singly bonded C-O polar groups on its surface. In this view, it is reasonable to argue that the grafting of calcium, carbonate and phosphate ions is enhanced under these conditions. In particular, this process is expected to be even more accentuated in the first days of exposure to 1.5 SBF. In fact, the incorporation of carbonate ions, as well as the secondary nucleation and crystal growth of the apatite-like nuclei would be plausibly favored by the presence of the C-O polar groups on diamond surface, producing a continuous and homogenous C-HA deposit as the immersion time in SBF increases.

4. Conclusions

The present research is devoted to investigating how the bioactivity of the diamond phase to precipitate carbonated hydroxyapatite from a physiological environment can be purposely tailored by the modulation of diamond surface chemistry and structural features. A HF-CVD method was employed to synthesize polycrystalline diamond films on titanium substrates. An oxidative treatment in air at 350 $^{\circ}\text{C}$ was adopted to functionalize the diamond surface with a 10% of singly bonded C-O groups. The growth of C-HA crystals by precipitation from a simulated body fluid was monitored by means of Raman spectroscopy analysis after regular periods of time from 3 to 20 days. The collected results pointed out the capability of the annealed diamond to support and promote the growth of a B-type C-HA with a carbonate content strictly close to that of human bone. Furthermore, the annealing treatment was found to enhance the deposition of C-HA with respect to bare titanium and as-grown PCD films. In particular, the SEM-EDX analyses corroborated that the employed method for the controlled introduction of C-O moieties on diamond surface is crucial to obtain continuous C-HA coatings with crystals showing morphology and chemical composition similar to those of the bone-mineral. Such findings make the annealed diamond system a valuable bioactive platform to be used as scaffold in the implantable prosthesis field.

Author Contributions: Conceptualization: R.C., E.T. and S.O.; methodology: R.C., E.T. and S.O.; formal analysis: R.C.; investigation: R.C., V.G. and F.M.; data curation: R.C., V.G. and E.T.; software: R.C. and F.M.; validation: E.T. and S.O.; writing—original draft preparation: R.C.; writing—review and editing: E.T. All authors have read and agreed to the published version of the manuscript.

Funding: No funding was received for conducting this study.

Data Availability Statement: The authors confirm that the data supporting the findings of this study are available within the article.

Acknowledgments: The authors acknowledge Maria Letizia Terranova for her encouragement and valuable suggestions, leading to the publication of this paper. The authors are grateful to Nanoshare Srl for the financial support of the SEM-EDX analyses performed at Center for Nanotechnology Applied to Industry (CNIS) of University of Rome “Sapienza”. The authors wish to thank Fondazione Bruno Kessler (FBK, Trento, Italy) for assistance with XPS measurements. R.C. is grateful to FBK for financial support.

Conflicts of Interest: The authors declare no conflict of interest.

References

1. Raymakers, J.; Haenen, K.; Maes, W. Diamond Surface Functionalization: From Gemstone to Photoelectrochemical Applications. *J. Mater. Chem. C* **2019**, *7*, 10134–10165. [[CrossRef](#)]
2. Panizza, M.; Cerisola, G. Application of Diamond Electrodes to Electrochemical Processes. *Electrochim. Acta* **2005**, *51*, 191–199. [[CrossRef](#)]
3. Politi, S.; Battistoni, S.; Carcione, R.; Montaina, L.; Macis, S.; Lupi, S.; Tamburri, E. PANI-Modified Ti-Doped CVD Diamond As Promising Conductive Platform to Mimic Bioelectricity Functions. *Adv. Mater. Interfaces* **2021**, *8*, 2101401. [[CrossRef](#)]
4. Tyszczyk-Rotko, K.; Jaworska, I.; Jedruchiewicz, K. Application of Unmodified Boron-Doped Diamond Electrode for Determination of Dopamine and Paracetamol. *Microchem. J.* **2019**, *146*, 664–672. [[CrossRef](#)]
5. Fox, K.; Palamara, J.; Judge, R.; Greentree, A.D. Diamond as a Scaffold for Bone Growth. *J. Mater. Sci. Mater. Med.* **2013**, *24*, 849–861. [[CrossRef](#)]
6. Baluchová, S.; Brycht, M.; Taylor, A.; Mortet, V.; Krůšek, J.; Dittert, I.; Sedláková, S.; Klimša, L.; Kopeček, J.; Schwarzová-Pecková, K. Enhancing Electroanalytical Performance of Porous Boron-Doped Diamond Electrodes by Increasing Thickness for Dopamine Detection. *Anal. Chim. Acta* **2021**, *1182*, 338949. [[CrossRef](#)]
7. Fox, K.; Mani, N.; Rifai, A.; Reineck, P.; Jones, A.; Tran, P.A.; Ramezannejad, A.; Brandt, M.; Gibson, B.C.; Greentree, A.D.; et al. 3D-Printed Diamond-Titanium Composite: A Hybrid Material for Implant Engineering. *ACS Appl. Bio Mater.* **2020**, *3*, 29–36. [[CrossRef](#)]
8. Fong, J.S.L.; Booth, M.A.; Rifai, A.; Fox, K.; Gelmi, A. Diamond in the Rough: Toward Improved Materials for the Bone–Implant Interface. *Adv. Healthc. Mater.* **2021**, *10*, 2100007. [[CrossRef](#)]
9. Booth, M.A.; Pope, L.; Sherrell, P.C.; Stacey, A.; Tran, P.A.; Fox, K.E. Polycrystalline Diamond Coating on 3D Printed Titanium Scaffolds: Surface Characterisation and Foreign Body Response. *Mater. Sci. Eng. C* **2021**, *130*, 112467. [[CrossRef](#)]
10. Hupert, M.; Muck, A.; Wang, J.; Stotter, J.; Cvackova, Z.; Haymond, S.; Show, Y.; Swain, G.M. Conductive Diamond Thin-Films in Electrochemistry. *Diam. Relat. Mater.* **2003**, *12*, 1940–1949. [[CrossRef](#)]
11. Dutta, G.; Siddiqui, S.; Zeng, H.; Carlisle, J.A.; Arumugam, P.U. The Effect of Electrode Size and Surface Heterogeneity on Electrochemical Properties of Ultrananocrystalline Diamond Microelectrode. *J. Electroanal. Chem.* **2015**, *756*, 61–68. [[CrossRef](#)] [[PubMed](#)]
12. Etemadi, H.; Yegani, R.; Babaeipour, V. Study on the Reinforcing Effect of Nanodiamond Particles on the Mechanical, Thermal and Antibacterial Properties of Cellulose Acetate Membranes. *Diam. Relat. Mater.* **2016**, *69*, 166–176. [[CrossRef](#)]
13. Tamburri, E.; Carcione, R.; Vitale, F.; Valguarnera, A.; Macis, S.; Lucci, M.; Terranova, M.L. Exploiting the Properties of Ti-Doped CVD-Grown Diamonds for the Assembling of Electrodes. *Adv. Mater. Interfaces* **2017**, *4*, 1700222. [[CrossRef](#)]
14. Reina, G.; Orlanducci, S.; Cairone, C.; Tamburri, E.; Lenti, S.; Cianchetta, I.; Rossi, M.; Terranova, M.L. Rhodamine/Nanodiamond as a System Model for Drug Carrier. *J. Nanosci. Nanotechnol.* **2015**, *15*, 1022–1029. [[CrossRef](#)] [[PubMed](#)]
15. Haubner, R. Low-Pressure Diamond: From the Unbelievable to Technical Products. *ChemTexts* **2021**, *7*, 10. [[CrossRef](#)]
16. Bhattacharyya, S.; Auciello, O.; Birrell, J.; Carlisle, J.A.; Curtiss, L.A.; Goyette, A.N.; Gruen, D.M.; Krauss, A.R.; Schlueter, J.; Sumant, A.; et al. Synthesis and Characterization of Highly-Conducting Nitrogen-Doped Ultrananocrystalline Diamond Films. *Appl. Phys. Lett.* **2001**, *79*, 1441–1443. [[CrossRef](#)]
17. Grausova, L.; Kromka, A.; Burdikova, Z.; Eckhardt, A.; Rezek, B.; Vacik, J.; Haenen, K.; Lisa, V.; Bacakova, L. Enhanced Growth and Osteogenic Differentiation of Human Osteoblast-like Cells on Boron-Doped Nanocrystalline Diamond Thin Films. *PLoS ONE* **2011**, *6*, e20943. [[CrossRef](#)]
18. Terranova, M.L.; Rossi, M.; Vitali, G. Structural Investigation of the Titanium/Diamond Film Interface. *J. Appl. Phys.* **1998**, *80*, 3552–3560. [[CrossRef](#)]
19. Mandal, S. Nucleation of Diamond Films on Heterogeneous Substrates: A Review. *RSC Adv.* **2021**, *11*, 10159–10182. [[CrossRef](#)]

20. Carcione, R.; Tamburri, E.; Bartali, R.; Speranza, G.; Micheli, V.; Pepponi, G.; Bellutti, P.; Terranova, M.L. On the route to produce conductive Ni-related color centers in CVD-grown diamond. *Multifunct. Mater.* **2019**, *2*, 035001. [[CrossRef](#)]
21. Terranova, M.L.; Piccirillo, S.; Sessa, V.; Compagnone, D.; Sbornicchia, P.; Rossi, M. Electrochemical Behaviour of Electrodes Assembled with Ti-Containing Diamond Films. *Diam. Relat. Mater.* **2001**, *10*, 627–630. [[CrossRef](#)]
22. Rifai, A.; Tran, N.; Reineck, P.; Elbourne, A.; Mayes, E.; Sarker, A.; Dekiwadia, C.; Ivanova, E.P.; Crawford, R.J.; Ohshima, T.; et al. Engineering the Interface: Nanodiamond Coating on 3D-Printed Titanium Promotes Mammalian Cell Growth and Inhibits Staphylococcus Aureus Colonization. *ACS Appl. Mater. Interfaces* **2019**, *11*, 24588–24597. [[CrossRef](#)] [[PubMed](#)]
23. Sur, D.; Tirado, P.; Alcantar, J.; Auciello, O.; Basim, G.B. Integration of Ultrananocrystalline Diamond (UNCD)-Coatings on Chemical-Mechanical Surface Nano-Structured (CMNS) Titanium-Based Dental Implants. *MRS Adv.* **2020**, *5*, 2261–2271. [[CrossRef](#)]
24. Shen, S.; Shen, W.; Liu, S.; Li, H.; Chen, Y.; Qi, H. First-Principles Calculations of Co-Doping Impurities in Diamond. *Mater. Today Commun.* **2020**, *23*, 100847. [[CrossRef](#)]
25. Li, S.; Wang, J.; Hu, M.; Li, M.; Liu, X.; Su, T.; Yu, K.; Han, F. The First Principle Study and Experimental of Boron Synergistic Sulfur Doping in Diamond. *Mater. Today Commun.* **2020**, *24*, 101021. [[CrossRef](#)]
26. Goss, J.P.; Briddon, P.R.; Jones, R.; Sque, S. Donor and Acceptor States in Diamond. *Diam. Relat. Mater.* **2004**, *13*, 684–690. [[CrossRef](#)]
27. Ödman, J.; Lekholm, U.; Jemt, T.; Brånemark, P.-I.; Thilander, B. Osseointegrated Titanium Implants—A New Approach in Orthodontic Treatment. *Eur. J. Orthod.* **1988**, *10*, 98–105. [[CrossRef](#)] [[PubMed](#)]
28. Jiang, G.; He, G. Enhancement of the Porous Titanium with Entangled Wire Structure for Load-Bearing Biomedical Applications. *Mater. Des.* **2014**, *56*, 241–244. [[CrossRef](#)]
29. Janson, O.; Gururaj, S.; Pujari-Palmer, S.; Karlsson Ott, M.; Strømme, M.; Engqvist, H.; Welch, K. Titanium Surface Modification to Enhance Antibacterial and Bioactive Properties While Retaining Biocompatibility. *Mater. Sci. Eng. C* **2019**, *96*, 272–279. [[CrossRef](#)]
30. Dallago, M.; Fontanari, V.; Torresani, E.; Leoni, M.; Pederzoli, C.; Potrich, C.; Benedetti, M. Fatigue and Biological Properties of Ti-6Al-4V ELI Cellular Structures with Various Arranged Cubic Cells Made by Selective Laser Melting. *J. Mech. Behav. Biomed. Mater.* **2018**, *78*, 381–394. [[CrossRef](#)]
31. Carcione, R.; Battistoni, S.; Palmieri, E.; Orlanducci, S.; Tamburri, E. Pretreatment Strategies of Titanium Substrates to Modulate the Electrochemical Properties of CVD-Grown Ti-Doped Diamond Electrodes for Dopamine Detection. *Surf. Coatings Technol.* **2023**, *467*, 129662. [[CrossRef](#)]
32. Battistoni, S.; Carcione, R.; Tamburri, E.; Erokhin, V.; Terranova, M.L.; Iannotta, S. A Ti-Doped Chemical Vapor Deposition Diamond Device as Artificial Synapse for Neuromorphic Applications. *Adv. Mater. Technol.* **2023**, *8*, 2201555. [[CrossRef](#)]
33. Jozwik, K.; Karczemska, A. The New Generation Ti6Al4V Artificial Heart Valve with Nanocrystalline Diamond Coating on the Ring and with Derlin Disc after Long-Term Mechanical Fatigue Examination. *Diam. Relat. Mater.* **2007**, *16*, 1004–1009. [[CrossRef](#)]
34. Papo, M.J.; Catledge, S.A.; Vohra, Y.K.; Machado, C. Mechanical Wear Behavior of Nanocrystalline and Multilayer Diamond Coatings on Temporomandibular Joint Implants. *J. Mater. Sci. Mater. Med.* **2004**, *15*, 773–777. [[CrossRef](#)]
35. Fries, M.D.; Vohra, Y.K. Nanostructured Diamond Film Deposition on Curved Surfaces of Metallic Temporomandibular Joint Implant. *J. Phys. D Appl. Phys.* **2002**, *35*, L105. [[CrossRef](#)]
36. Aspenberg, P.; Anttila, A.; Konttinen, Y.T.; Lappalainen, R.; Goodman, S.B.; Nordsletten, L.; Santavirta, S. Benign Response to Particles of Diamond and SiC: Bone Chamber Studies of New Joint Replacement Coating Materials in Rabbits. *Biomaterials* **1996**, *17*, 807–812. [[CrossRef](#)] [[PubMed](#)]
37. Bacakova, L.; Kopova, I.; Stankova, L.; Liskova, J.; Vacik, J.; Lavrentiev, V.; Kromka, A.; Potocky, S.; Stranska, D. Bone Cells in Cultures on Nanocarbonbased Materials for Potential Bone Tissue Engineering: A Review. *Phys. Status Solidi (A)* **2014**, *211*, 2688–2702. [[CrossRef](#)]
38. Carcione, R.; Politi, S.; Iacob, E.; Potrich, C.; Lunelli, L.; Vanzetti, L.E.; Bartali, R.; Micheli, V.; Pepponi, G.; Terranova, M.L.; et al. Exploring a New Approach for Regenerative Medicine: Ti-Doped Polycrystalline Diamond Layers as Bioactive Platforms for Osteoblast-like Cells Growth. *Appl. Surf. Sci.* **2021**, *540*, 148334. [[CrossRef](#)]
39. Ali, M.; Ali, F.; Yang, B.; Abbas, A. A Comprehensive Account of Biomedical Applications of CVD Diamond Coatings. *J. Phys. D Appl. Phys.* **2021**, *54*, 443001. [[CrossRef](#)]
40. Strąkowska, P.; Beutner, R.; Gnyba, M.; Zielinski, A.; Scharnweber, D. Electrochemically Assisted Deposition of Hydroxyapatite on Ti6Al4V Substrates Covered by CVD Diamond Films—Coating Characterization and First Cell Biological Results. *Mater. Sci. Eng. C* **2016**, *59*, 624–635. [[CrossRef](#)]
41. Rifai, A.; Tran, N.; Lau, D.W.; Elbourne, A.; Zhan, H.; Stacey, A.D.; Mayes, E.L.H.; Sarker, A.; Ivanova, E.P.; Crawford, R.J.; et al. Polycrystalline Diamond Coating of Additively Manufactured Titanium for Biomedical Applications. *ACS Appl. Mater. Interfaces* **2018**, *10*, 8474–8484. [[CrossRef](#)] [[PubMed](#)]
42. El-wassefy, N.A.; Hammouda, I.M.; Habib, A.N.E.-D.A.; El-awady, G.Y.; Marzook, H.A. Assessment of Anodized Titanium Implants Bioactivity. *Clin. Oral Implants Res.* **2014**, *25*, e1–e9. [[CrossRef](#)] [[PubMed](#)]
43. Kim, H.M.; Miyaji, F.; Kokubo, T.; Nishiguchi, S.; Nakamura, T. Graded Surface Structure of Bioactive Titanium Prepared by Chemical Treatment. *J. Biomed. Mater. Res.* **1999**, *45*, 100–107. [[CrossRef](#)]
44. Kizuki, T.; Matsushita, T.; Kokubo, T. Antibacterial and Bioactive Calcium Titanate Layers Formed on Ti Metal and Its Alloys. *J. Mater. Sci. Mater. Med.* **2014**, *25*, 1737–1746. [[CrossRef](#)] [[PubMed](#)]

45. Wopenka, B.; Pasteris, J.D. A Mineralogical Perspective on the Apatite in Bone. *Mater. Sci. Eng. C* **2005**, *25*, 131–143. [[CrossRef](#)]
46. Sotiropoulou, P.; Fountos, G.; Martini, N.; Koukou, V.; Michail, C.; Kandarakis, I.; Nikiforidis, G. Bone Calcium/Phosphorus Ratio Determination Using Dual Energy X-ray Method. *Phys. Medica* **2015**, *31*, 307–313. [[CrossRef](#)]
47. Mohd Pu'ad, N.A.S.; Koshy, P.; Abdullah, H.Z.; Idris, M.I.; Lee, T.C. Syntheses of Hydroxyapatite from Natural Sources. *Heliyon* **2017**, *5*, e01588. [[CrossRef](#)]
48. Haberko, K.; Bućko, M.M.; Brzezińska-Miecznik, J.; Haberko, M.; Mozgawa, W.; Panz, T.; Pyda, A.; Zarebski, J. Natural Hydroxyapatite—Its Behaviour during Heat Treatment. *J. Eur. Ceram. Soc.* **2006**, *26*, 537–542. [[CrossRef](#)]
49. Atemni, I.; Ouafi, R.; Hjouji, K.; Mehdaoui, I.; Ainane, A.; Ainane, T.; Taleb, M.; Rais, Z. Extraction and Characterization of Natural Hydroxyapatite Derived from Animal Bones Using the Thermal Treatment Process. *Emergent Mater.* **2023**, *6*, 551–560. [[CrossRef](#)]
50. Kokubo, T.; Kushitani, H.; Sakka, S.; Kitsugi, T.; Yamamuro, T. Solutions Able to Reproduce In Vivo Surface-structure Changes in Bioactive Glass-ceramic A-W3. *J. Biomed. Mater. Res.* **1990**, *24*, 721–734. [[CrossRef](#)]
51. Ferrari, A.; Robertson, J. Interpretation of Raman Spectra of Disordered and Amorphous Carbon. *Phys. Rev. B* **2000**, *61*, 14095–14107. [[CrossRef](#)]
52. Ferrari, A.C.; Robertson, J. Resonant Raman Spectroscopy of Disordered, Amorphous, and Diamondlike Carbon. *Phys. Rev. B* **2001**, *64*, 075414. [[CrossRef](#)]
53. Ferrari, A.C.; Robertson, J. Raman Spectroscopy of Amorphous, Nanostructured, Diamondlike Carbon, and Nanodiamond. *Philos. Trans. R. Soc. London. Ser. A Math. Phys. Eng. Sci.* **2004**, *362*, 2477–2512. [[CrossRef](#)] [[PubMed](#)]
54. Vorlíček, V.; Rosa, J.; Vaněček, M.; Nesládek, M.; Stals, L.M. Quantitative Study of Raman Scattering and Defect Optical Absorption in CVD Diamond Films. *Diam. Relat. Mater.* **1997**, *6*, 704–707. [[CrossRef](#)]
55. Liu, X.; Lu, P.; Wang, H.; Ren, Y.; Tan, X.; Sun, S.; Jia, H. Morphology and Structure of Ti-Doped Diamond Films Prepared by Microwave Plasma Chemical Vapor Deposition. *Appl. Surf. Sci.* **2018**, *442*, 529–536. [[CrossRef](#)]
56. Alba, G.; Eon, D.; Villar, M.P.; Alcántara, R.; Chicot, G.; Cañas, J.; Letellier, J.; Pernot, J.; Araujo, D. H-Terminated Diamond Surface Band Bending Characterization by Angle-Resolved XPS. *Surfaces* **2020**, *3*, 61–71. [[CrossRef](#)]
57. Merel, P.; Tabbal, M.; Chaker, M.; Moisa, S.; Margot, J. Direct Evaluation of the Sp³ Content in Diamond-like-Carbon Films by XPS. *Appl. Surf. Sci.* **1998**, *136*, 105–110. [[CrossRef](#)]
58. Park, C.K.; Chang, S.M.; Uhm, H.S.; Seo, S.H.; Park, J.S. XPS and XRR Studies on Microstructures and Interfaces of DLC Films Deposited by FCVA Method. *Thin Solid Films* **2002**, *420*, 235–240. [[CrossRef](#)]
59. Ferro, S.; Dal Colle, M.; De Battisti, A. Chemical Surface Characterization of Electrochemically and Thermally Oxidized Boron-Doped Diamond Film Electrodes. *Carbon* **2005**, *43*, 1191–1203. [[CrossRef](#)]
60. Antonakos, A.; Liarokapis, E.; Leventouri, T. Micro-Raman and FTIR Studies of Synthetic and Natural Apatites. *Biomaterials* **2007**, *28*, 3043–3054. [[CrossRef](#)]
61. Awonusi, A.; Morris, M.D.; Tecklenburg, M.M.J. Carbonate Assignment and Calibration in the Raman Spectrum of Apatite. *Calcif. Tissue Int.* **2007**, *81*, 46–52. [[CrossRef](#)] [[PubMed](#)]
62. Okagbare, P.I.; Begun, D.; Tecklenburg, M.; Awonusi, A.; Goldstein, S.A.; Morris, M.D. Noninvasive Raman Spectroscopy of Rat Tibiae: Approach to In Vivo Assessment of Bone Quality. *J. Biomed. Opt.* **2012**, *17*, 090502. [[CrossRef](#)] [[PubMed](#)]
63. Yasar, O.F.; Liao, W.C.; Mathew, R.; Yu, Y.; Stevensson, B.; Liu, Y.; Shen, Z.; Edén, M. The Carbonate and Sodium Environments in Precipitated and Biomimetic Calcium Hydroxy-Carbonate Apatite Contrasted with Bone Mineral: Structural Insights from Solid-State NMR. *J. Phys. Chem. C* **2021**, *125*, 10572–10592. [[CrossRef](#)]
64. Nosenko, V.V.; Yaremko, A.M.; Dzhagan, V.M.; Vorona, I.P.; Romanyuk, Y.A.; Zatovsky, I.V. Nature of Some Features in Raman Spectra of Hydroxyapatite-Containing Materials. *J. Raman Spectrosc.* **2016**, *47*, 726–730. [[CrossRef](#)]
65. Taylor, E.A.; Mileti, C.J.; Ganesan, S.; Kim, J.H.; Donnelly, E. Measures of Bone Mineral Carbonate Content and Mineral Maturity/Crystallinity for FT-IR and Raman Spectroscopic Imaging Differentially Relate to Physical–Chemical Properties of Carbonate-Substituted Hydroxyapatite. *Calcif. Tissue Int.* **2021**, *109*, 77–91. [[CrossRef](#)]
66. Spizzirri, P.G.; Cochrane, N.J.; Praver, S.; Reynolds, E.C. A Comparative Study of Carbonate Determination in Human Teeth Using Raman Spectroscopy. *Caries Res.* **2012**, *46*, 353–360. [[CrossRef](#)]
67. Ishikawa, K.; Hayashi, K. Carbonate Apatite Artificial Bone. *Sci. Technol. Adv. Mater.* **2021**, *22*, 683–694. [[CrossRef](#)]
68. Nagai, H.; Kobayashi-Fujioka, M.; Fujisawa, K.; Ohe, G.; Takamaru, N.; Hara, K.; Uchida, D.; Tamatani, T.; Ishikawa, K.; Miyamoto, Y. Effects of Low Crystalline Carbonate Apatite on Proliferation and Osteoblastic Differentiation of Human Bone Marrow Cells. *J. Mater. Sci. Mater. Med.* **2015**, *26*, 1–8. [[CrossRef](#)]
69. Sadowska, J.M.; Wei, F.; Guo, J.; Guillem-Marti, J.; Ginebra, M.P.; Xiao, Y. Effect of Nano-Structural Properties of Biomimetic Hydroxyapatite on Osteoimmunomodulation. *Biomaterials* **2018**, *181*, 318–332. [[CrossRef](#)]

Disclaimer/Publisher's Note: The statements, opinions and data contained in all publications are solely those of the individual author(s) and contributor(s) and not of MDPI and/or the editor(s). MDPI and/or the editor(s) disclaim responsibility for any injury to people or property resulting from any ideas, methods, instructions or products referred to in the content.